Solid state reactions and defects in Verneuil laser rubies

Autor(en): **Borer, W.J. / Günthard, Hs.H. / Ballmer, P.**

Objekttyp: **Article**

Zeitschrift: **Helvetica Physica Acta**

Band (Jahr): **43 (1970)**

Heft 1

PDF erstellt am: **13.09.2024**

Persistenter Link: https://doi.org/10.5169/seals-114158

Solid State Reactions and Defects in Verneuil Laser Rubies

by **W. J. Borer**[1]) and **Hs. H. Günthard**

Swiss Federal Institute of Technology, Department of Physical Chemistry, 8006 Zurich, Switzerland

and **P. Ballmer**

Djévahirdjian S.A., Monthey, Switzerland

(25. IX. 69)

Abstract. The defects characteristic for a certain type of ruby ('brown ruby') with very low laser efficiency were investigated by optical, infrared, thermoluminescence, and ESR spectra, and by analytical methods of trace detection. Significant correlation of these defects with impurities present in the brown state of ruby was established. The defects may be eliminated by appropriate heat treatments, which were found to be associated with several solid state reactions as well as with a considerable increase of laser efficiency. The typical UV absorption spectrum is interpreted as the crystal field spectrum of Cr^{+3} on interstitial sites. This view is supported by the results of extended computations of crystal field spectra.

I. Introduction

Rubies and corundum have hitherto been objects of several investigations. In most of these publications the authors discuss defects and color centers, which were produced by UV-, reactor- or gamma-irradiation. Hunt and Schuler [1] reported on two absorption bands at 230 and 400 nm. These bands could be annealed at 1000 °C. A weak thermoluminescence was observed at about 500 °C. The absorption band at 400 nm was also investigated by Levy [2, 3]. Following reactor irradiation, five or six further bands arise besides the already known bands. These, however, were much weaker. Levy analyzed his absorption spectra, assuming a gaussian line shape. Mitchell, Rigden and Townsend [4] investigated the anisotropy of the bands produced by neutron and electron irradiation. Gabrysh et al. [5, 6] analyzed luminescence phenomena on gamma-irradiated corundum. Gamble et al. [7] irradiated sapphire in the reactor, and with gamma-rays at low temperature. They proposed O^+ on an interstitial site as color center. Bartram et al. [8] also investigated sapphire after gamma and reactor irradiation. With the help of electron resonance and optical spectroscopy they discussed O^+ and O^0 at interstitial sites, as well as O^- combined

[1]) Present address: Department of Electrical Engeneering, University of Rhode Island, Kingston, Rhode Island 02881, USA.

with a charge deficient cation. This color center gives rise to an absorption band at approximately 430 nm.

Luminescence and thermoluminescence phenomena with X-ray irradiated sapphire and ruby were reported by Sujak and Niklas [9, 10]. They measured thermoluminescence maxima at 180, 280 and 380 °C. Lehmann and Guenthard [11] investigated the luminescence and absorption of flash light excited sapphire. After excitation with flash light they found absorption bands at 206, 255 and 400 nm. An other broad absorption band was found after UV-irradiation by means of a Xenon lamp. Muller and Guenthard [12] report on oxydation and reduction processes in Co- and Ni-doped sapphire. Cutler et al. [13] showed that the absorption band at 255 nm can be produced by annealing the sapphire in oxygen atmospere, and that annealing in hydrogen atmosphere eliminated this band.

R. C. Pastor et al. [14–17] published several papers referring to the Verneuil process itself. They concern steady state studies and discussions on burn-out, and surface and bulk states of the additives in the Al_2O_3 powder.

A general feature of the whole body of the work on color centers in sapphire and ruby seems to be the fact that very little attention has been paid to the effects of impurities present in the crystals, although they might be important. In this paper we report on investigations with Verneuil laser rubies. Some of these rubies show, in addition to the color produced by the substitutional Cr^{+3}-ions, whose spectrum is well known [18], two additional color centers which were found to be associated with a poor efficiency of these rubies in the laser. The centers are characterized by an absorption band at 315 nm, and a very broad absorption band near 480 nm, respectively. About 30% of the investigated rubies show these color centers.

For characterization of these color centers UV-, optical-, IR- and ESR-spectroscopy were applied. Furthermore several methods for determination of small amounts of impurities other than Cr were applied, such as neutron activation analysis, electron microprobe analysis and X-ray spectroscopy. Annealing experiments in vacuum, and in reducing and oxydizing atmosphere were performed.

For the 315 nm absorption band a model will be suggested and veryfied by a crystal field calculation.

Part II will give a description of the experimental methods and the samples which were used.

In part III we present the experimental results.

Part IV gives a general discussion of models which may be suggested for the observed defects. The models are discussed with the help of crystal field theory and thermodynamic processes.

II. Experimental

2.1 *Ruby Samples*

A sample of about twenty ruby laser rods was available for the different experiments. These ruby rods were of cylindrical shape with diameters between 6 and 14 mm and leths between 6 and 12 cm. The angle between the rod axis and the optical *c*-axis was either 60 degrees or 90 degrees. Two or three disks (ca. 2 mm thick)

were cut from each of these laser rods, polished on both sides and used for spectroscopic and analytical investigations. The remainder of the laser rods was again polished to laser quality.

All these ruby rods showed a relatively bad laser efficiency, or no laser effect at all. The as-grown rubies may, according to their spectra in the visible and UV region, be divided in two groups:

The first group consists of rubies which have an absorption spectrum not essentially different from the spectrum known as originating from Cr^{+3} in corundum, i.e. with pink color. The rubies of this group will be called 'perfect' in the following text.

The second group of rubies shows a brown color, with which an absorption band near 480 nm is associated. Also, all rubies of this group exhibit an absorption band at 315 nm. We shall call these rubies 'brown' in the following text.

2.2 *Visible and UV Absorption Spectra*

Absorption spectra between 200 and 700 nm were recorded with a Beckman-DK-2 double beam spectrometer. Laser rods or sample disks were used for this purpose.

2.3 *Electron Spin Resonance Spectra*

A K-band superheterodyne spectrometer with a sensitivity of ca. $2 \cdot 10^{10}$ spins was used. This instrument is described in a publication by P. E. Schmid et al. [19]. Cylindrical rods of 1 mm diameter and 10 mm length with optical *c*-axis perpendicular to the rod axis were used for the ESR measurements. All ESR measurements were performed at room temperature.

2.4 Thermoluminescence measurements were made with a double beam instrument consisting of a Beckman DK-2 sample compartment and a Perkin-Elmer Monochromator Model 99 equipped with a photomultiplier. Maximum operating temperature of the instrument was approx. 600 °C [2]). In most cases thermoluminescence intensity was very low and required considerable care for reliable detection. In particular the heat radiation from the sample had to be compensated by the double beam system. Minimum measurable trap depth was approx. 0.5 eV.

2.5 For investigation of the correlation of laser efficiency with color center concentration a conventional laser with cylindrical mirror and external optical cavity mirrors was used, allowing a maximum pumping energy of 3.7 kJ. Relative laser output energy was measured with a photocell and electronic integrator.

2.6 Thermal treatments up to 1600 °C were made in an oven equipped with commercial Al_2O_3 tubes of highest available purity. In order to control the atmosphere in which the ruby rods were annealed the alox tubes were connected either to a gas flow apparatus or to a vacuum system. The use of a flow system proved to be essential in order to avoid uncontrolled diffusion at the high temperature applied.

[2]) For details of the thermoluminescence set up cf. Ref. [20].

2.7 As mentionned above, considerable effort was made to obtain information about nature and amount of impurities present in the rubies. Since chemical analysis of trace impurities seems to be very difficult in sapphire and ruby owing to their chemical inertness, only non-destructive methods were applied. It was found, that relatively reliable and complete information could be obtained by neutron activation analysis (NA), the electron microprobe (EMP) and by X-ray spectroscopy (XRS). In this paper only relevant results of the analytical work will be given[3]). However, a few remarks with respect to error limits should be made.

i. In the case of EMP the time for a preset number of counts was measured. In order to define the mean and root mean square a modified gamma distribution was applied, for details the reader is referred to Ref. [20].

ii. For NA and XRS, count number in a fixed time was measured, hence the usual poisson distribution for definition of mean and variance applies.

III. Results

3.1 *Trace Analysis Results*

The results of the chemical analytical investigation of the rubies are collected in Table 1 and may be summarized as follows:

i. By the annealing process obviously the concentration of Na and K are reduced; in particular the decrease of K is significant. Figure 1 shows the K concentration profile in a ruby with pink peripheral zone and brown core. The photograph of the ruby, Figure 2, clearly shows the brown core (dark) in contrat to the pink peripheral part.

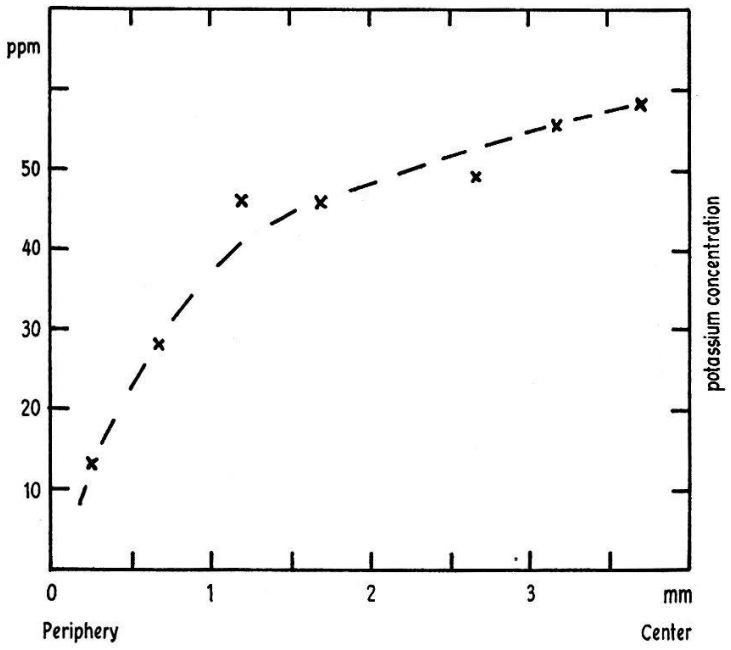

Figure 1
Potassium concentration along a diameter in a partially annealed brown ruby (with brown core)*).

*) C.f. Figure 2.

[3]) A detailed report of the analytical work will be published elsewhere.

ii. The concentration of other impurities than Na and K is not significantly affected by annealing.

Table 1
Results of trace analysis

Element	Ruby No.	Concentration [ppm] brown	annealed[1])	Detection limit [ppm]	Significance of difference[2])	Method[3])
F	132	<100	<100	100	no	EMP
Na	130	31 ± 14	24 ± 10	10	no[4])	EMP
Na	131	56 ± 5	49 ± 6	10	no[4])	EMP
Na	132	26 ± 12	23 ± 12	10	no[4])	EMP
Mg[5])	130	33 ± 6	52 ± 7	10	no	EMP
Mg[5])	130	54 ± 7	85 ± 9	10	no	EMP
Mg	131	<15	41 ± 16	15	yes	EMP
Si[6])	130	<20	36 ± 20	20	yes	EMP
Cl	130	not detectable				any
K	130	58 ± 10	<10	10	yes	EMP
Ca	130	5	7	1	no	XRS
Sc	130	<1	<1	1	no	XRS
Ti	131	<10	<10	10	no	EMP
Ti	131	3	3	1	no	XRS
V	131	<10	<10	10	no	EMP
V	131	<2	<2	2	no	XRS
Cr	130	630 ± 35	580 ± 35[7])	35	no	EMP
Mn	130	25 ± 16	31 ± 16	15	no	EMP
Mn	130	10	8	7	no	XRS
Fe	131	25 ± 12	25 ± 12	15	no	EMP
Fe	130	5	5	2	no	NA
Fe	130	30 ± 2	29 ± 2	1	no	XRS
Co	131	<0.005	<0.005	0.005	no	NA
Co	131	<2	<2	2	no	XRS
Ni	130	<2	<2	2	no	XRS
Cu	130	9 ± 5	13 ± 5	5	no	EMP
Cu	131	23 ± 5	33 ± 5	5	yes	EMP
Cu	132	24 ± 5	25 ± 5	5	no	EMP
Cu	130	5	5	0.004	no	NA
Cu	130	4	3	2	no	XRS
Zn	130	<2	<2	2	no	XRS
Sn	130	<3	4	3	no	XRS
Sr	130	<5	<5	5	no	XRS

[1]) Annealed or perfect rubies have been compared, as well as partially annealed rubies with a brown core in their central region.
[2]) «Yes» or «no» indicate, if there is a significant difference between brown and annealed (resp. perfect) or not.
[3]) EMP = electron microprobe, XRS = X-ray spectroscopy, NA = neutron activation analysis.
[4]) By pooling the results for Na a significance may be established.
[5]) Measurements on the same sample, but with different calibration samples.
[6]) Surface effects may be implied.
[7]) This concentration is normal for laser rubies.

iii. The total content of impurity elements which are to be expected to be reduced by H_2 to lower valence states, or oxydized by O_2 to higher valence states, i.e. Ti, V, Mn, Fe, Co, Ni, Cu, amounts to approx. 50 ppm.

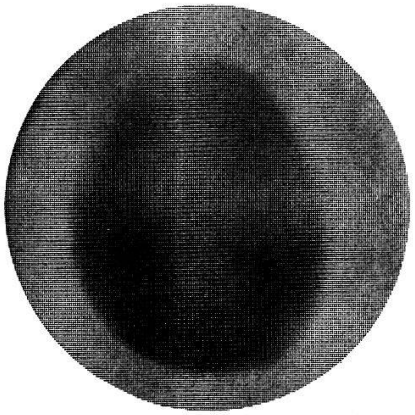

Figure 2
Photograph of partially annealed ruby with brown core.

Although growth of these rubies was made under carefully controlled conditions, Table 2 shows that generally the amount of impurities present is considerable. As will be discussed below, both the alcali and transition elements besides Cr play an important role in the behavior of the rubies under high temperature conditions.

Table 2
Trap depth of UV induced defects in ruby

Ruby No.	Trap depth [in eV] Urbach formula [20]	Initial rise [21]	Halperin [22]
110	1.45		2.6
111	1.45	1.5[1])	2.6
112	1.45		1.7
114	1.45	1.2[2])	1.8

[1]) Average among 8 experiments with the same sample.
[2]) Value too low owing to contribution of a relatively large glow peak at 310 °C.

3.2 *Effects of annealing on absorption spectra (ultraviolet (UV), visible (VIS) and infrared (IR)).*

3.2.1 In Figure 3 the UV and VIS spectra of 'brown' and 'perfect' ruby are shown. The most remarkable differences are the 315 nm absorption and an absorption near 480 nm, which both are characteristic of the 'brown' rubies. In the case of the 480 nm absorption, it is difficult to decide whether one or several absorption bands are involved. The 480 nm band also occurs in corundum (without Cr^{+3} dopant). The 315 nm absorption has not been observed by other workers in ruby and so far has not been found in sapphire.

3.2.2 'Brown' rubies were subjected to anyone of the following three different treatments:

i. annealing at 1550 °C in vacuum,

ii. annealing at 1550 °C in H_2 flow,

iii. annealing at 1550 °C in O_2 flow.

The same change in the absorption spectra was observed: The absorptions at 315 and 480 nm disappeared, and the resulting absorption spectrum was identical with the one of perfect ruby shown in Figure 3.

3.2.3 If treatment in H_2 flow at 1550 °C is made with

i. as-grown brown rubies,

ii. as-grown perfect rubies,

iii. rubies treated in oxygen flow during 44 hours,

iv. rubies treated in oxygen flow during 80 hours,

then with the exception of i. no change in the UV/VIS spectra was observed.

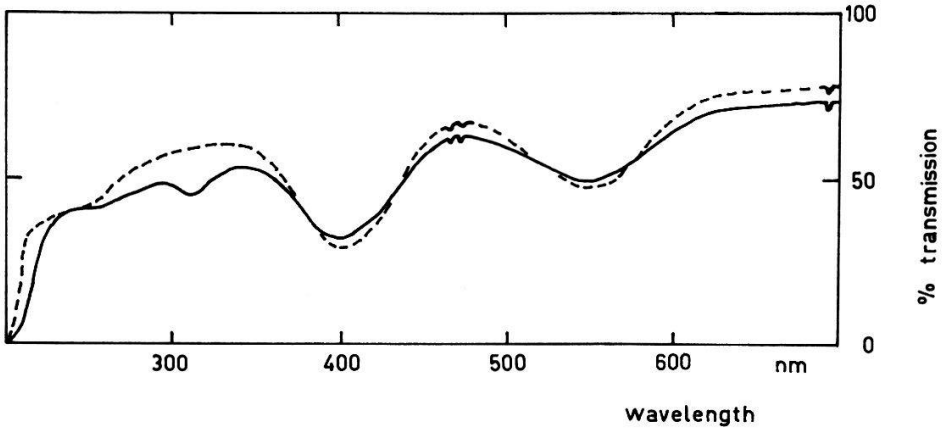

Figure 3
Absorption spectrum of brown ruby (solid line) and of perfect, respectively annealed ruby (dashed line).

3.2.4 If the H_2 flow treatment was preceded by an oxygen treatment, all rubies showed IR absorption bands at 3309, 3232 and 3184 cm^{-1}. Figure 4 demonstrates a typical IR absorption spectrum. If the treatment was not preceded by an O_2 treatment, no IR absorption bands were detectable. The concentration of hydrogen

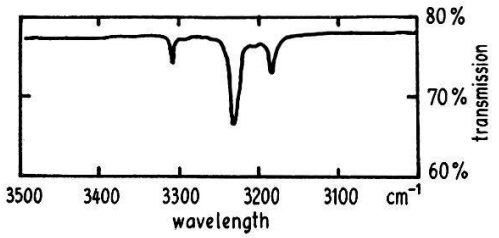

Figure 4
Infrared absorption spectrum of ruby annealed in hydrogen.

incorporated in the crystals was found to be approximately proportional to the duration of the O_2 treatment. However, no attempts have been made to reach saturation. Based on measurements of the IR bands by R. Mueller [12] the hydrogen concentration observed in rubies amounts to approximately 50–100 ppm.

3.3 *UV Irradiation Effects and Thermoluminescence*

3.3.1 Brown and perfect as-grown rubies and vacuum annealed rubies have been UV irradiated with a Xenon lamp during about 30 minutes. The following effects on the absorption spectrum 200–700 nm have been observed:

i. all investigated rubies showed a decrease of transmission near 350, 400 and 480 nm.

ii. perfect and annealed rubies showed a decrease of transmission in the 200–350 nm region nearly independent of the wavelength.

iii. brown rubies showed – besides the effects mentionned sub i. a decrease of transmission near 230, 255 and 285 nm, and an increase of transmission near

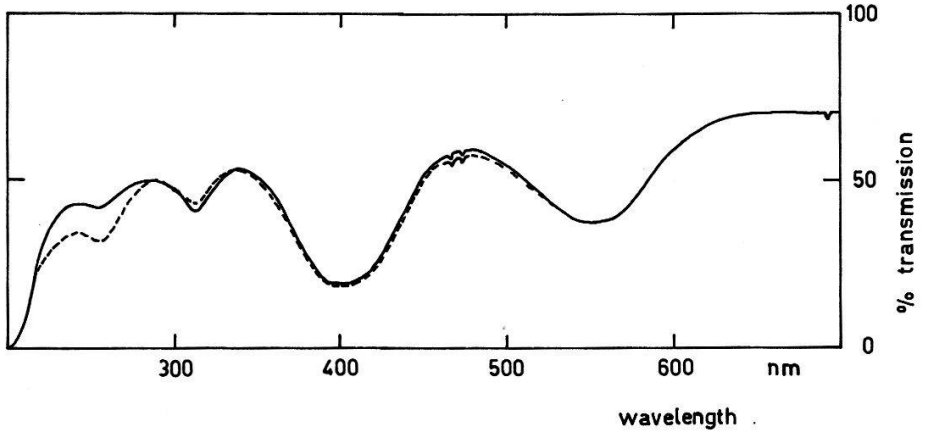

Figure 5
Absorption spectrum of brown ruby before UV irradiation (solid line) and after UV irradiation (dashed line).

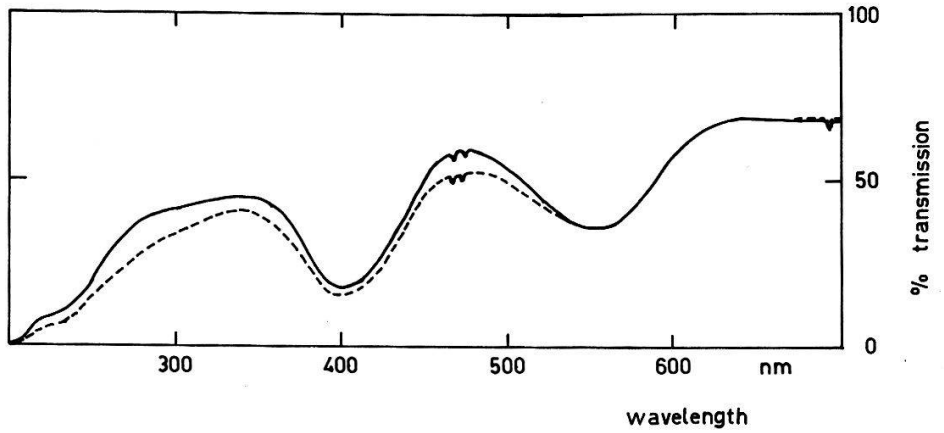

Figure 6
Absorption spectra of annealed or perfect ruby before UV irradiation (solid line) and after UV irradiation (dashed line).

315 nm. In the 600–700 nm region a decrease of transmission independent of wavelength was observed. Some of the effects are very small and difficult to measure quantitatively owing to serious experimental problems arising when reliable difference spectra are to be measured. Figures 5 and 6 show the typical UV induced spectra obtained in comparison with the absorption spectra of the same ruby annealed after UV irradiation.

3.3.2 The UV induced color centers may be reversibly annealed, the annealing process being associated with thermoluminescence emission. This thermoluminescence may be characterized as follows:

i. all rubies of the sample investigated showed glow peaks at the same temperature. A typical case is represented by Figure 7, which reveals a major glow peak at 450 °C. Besides this one weak peaks were observed reproducibly at 370 and 510 °C.

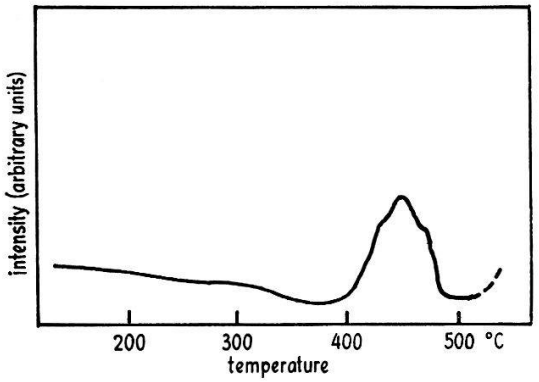

Figure 7
Typical glow peak of UV irradiated ruby.

ii. the emission spectrum also was the same for all rubies, as shown in Figure 8, characterized by a maximum of emitted intensity at 685 ± 15 nm. The main contribution to the errors of the peak wavelength results from the spectral slit width used.

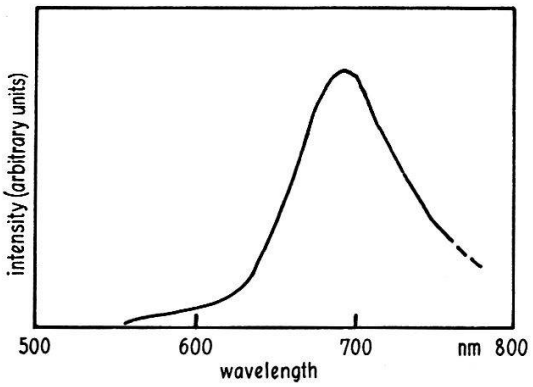

Figure 8
Spectral thermoluminescence emission of UV irradiated ruby.

iii. trap depth of the UV induced defects was determined by three different methods described in literature [21–23]. The results are collected in Table 2.

3.4 *Correlation of Defects with Laser Efficiency*

A marked difference was found between brown and annealed rubies with respect to laser efficiency. Using the laser setup described sub 2.5, the laser threshold and output was measured in comparison to a standard laser ruby operated under the same conditions. Laser characteristics were measured for both the brown and the annealed state; annealing was performed at 1550 °C for 90 h in vacuum. The results are listed in Table 3 for 3 typical rubies out of the sample.

Table 3 clearly shows:

i. brown rubies either have a very high threshold or do not lase at all for pump energies $\leqslant 3.7$ kJ.

ii. brown rubies after annealing exhibit much lower threshold and higher output energy at a given pump energy.

3.5 Measurement of line shape of the Cr^{+3} ESR-signal of brown and annealed ruby yielded no detectable differences. Also no significant difference of the intensity of this signal in the two states of the rubies could be observed (accuracy approx. 10%). Furthermore no other signal in the range 2 to 13 kGauss was found with the K-band spectrometer.

IV. Discussion

The discussion of the experimental facts is divided into the following parts:

4.1 General model for the physical structure of the defects for brown rubies and for UV-irradiated rubies.

4.2 Solid state oxydation-reduction (redox) reactions involved in the annealing processes of brown rubies.

4.3 Spectra of UV induced defects.

4.4 Crystal field theory of UV-VIS-spectra of typical defects of brown rubies.

4.1 The model for the defects of brown rubies which will be suggested, is based upon the sequence of states and processes schematized by Figure 9. As may be seen from this figure, a complicated structure of the typical defect of brown ruby has to be chosen, if it is to be compatible with all experimental facts. However, the number of a priori possible models may be efficiently reduced by thermodynamic considerations. Most of the processes occuring in Figure 9 involve chemical reactions between gaseous species and particles incorporated in the crystal structure.

4.2 A number of solid state redox processes are involved in the model suggested in Figure 9. Any such process should be thermodynamically possible. In order to get information about the free enthalpy of such reactions, data are required both about gaseous and dissolved species. Whereas for the former data are available [24–26], chemical thermodynamic data of charged and uncharged particles like O^0, O^-, O^{-2}, M^{+z+1}, Cr^{+3}, H^+ and K^+ on substitutional and interstitial sites ought to be derived. Our calculation of these data will be restricted to 0 K; therefore chemical reaction

Table 3
Laser output energy and threshold of rubies in the brown and annealed state

Ruby No.	brown (as-grown) input energy[1])	output energy	threshold	annealed input energy	output energy	theshold
	1.55	0.65		1.55	0.8	
	1.96	0.75		1.95	1.0	
130	2.37	0.82	3.6	2.40	1.1	2.6
	2.76	0.85		2.64	1.6[a])	
	3.16	0.97		2.90	2.8[a])	
	3.60	1.10		3.16	3.6[a])	
				3.44	4.2[a])	
	1.96	0.37		1.54	0.4	
	2.17	0.42		1.95	0.5	
	2.40	0.45		2.40	0.6	
131	2.66	0.48	3.6	2.64	1.0[a])	2.6
	2.90	0.50		2.90	1.8[a])	
	3.20	0.65		3.16	2.8[a])	
	3.50	0.7		3.40	3.3[a])	
				3.65	4.0[a])	
	1.18	0.28		1.99	0.35	
	1.74	0.35		2.64	0.5	
132	2.40	0.5		2.90	1.4[a])	2.75
	3.20	0.65	3.2	3.16	2.3[a])	
	3.50	1.6[a])		3.60	2.7[a])	
				1.70	0.5	1.73
				1.80	1.5[a])	
109[2])				1.90	2.25[a])	
				2.00	2.85[a])	
				2.10	3.35[a])	

[a]) Laser spikes were observed on the oscilloscope.
[1]) Input energy and thesholds are given in kJoule, whereas the output energies are given in arbitrary units.
[2]) Ruby 109 is a «perfect» standard ruby which was measured for comparison.

energies $\Delta U^0(0)$ derived from crystal field potentials may be considered reliable, if $|\Delta U^0(0)|$ is greater than about 4 eV. Furthermore only the Coulomb contribution to the crystal field potential, which is the dominant part, has been used. Computation of this has been made based on published data for the sapphire structure [27] considered as a point charge system. Contributions to the energy originating from distortion of the Al_2O_3 lattice by the various defects are neglected, too. Grimes and Rice have shown by calculation of a model that the order of magnitude of such lattice relaxation energies does not exceed 1 eV. Details about computation procedures and results for the crystal potential at various sites will be given in section 4.4.1.

Table 4 gives a collection of relevant thermodynamic data for the gaseous species involved in the model presented in Figure 9. Using the crystal field potential

expansion coefficients listed in Table 6 and the data given in Table 4, the reaction energies compiled in Table 5 are derived.

One important remark has to be made with respect to all energies of reactions, in which H^+ is taking part. From infrared spectra it has been derived that the proton is located on a line connecting O^{-2} ions sitting in two layers adjacent to the Al site [12]. No experimental information is available on the distance of the proton from the oxygen nuclei. In order to get a closer idea about possible proton locations along the O^{-2}–O^{-2} line, the crystal field potential was calculated along this line and on a line connecting two Al sites located on adjacent triads. The result is given in Figure 10, which shows a saddle point of the crystal field potential in the intersection of the two

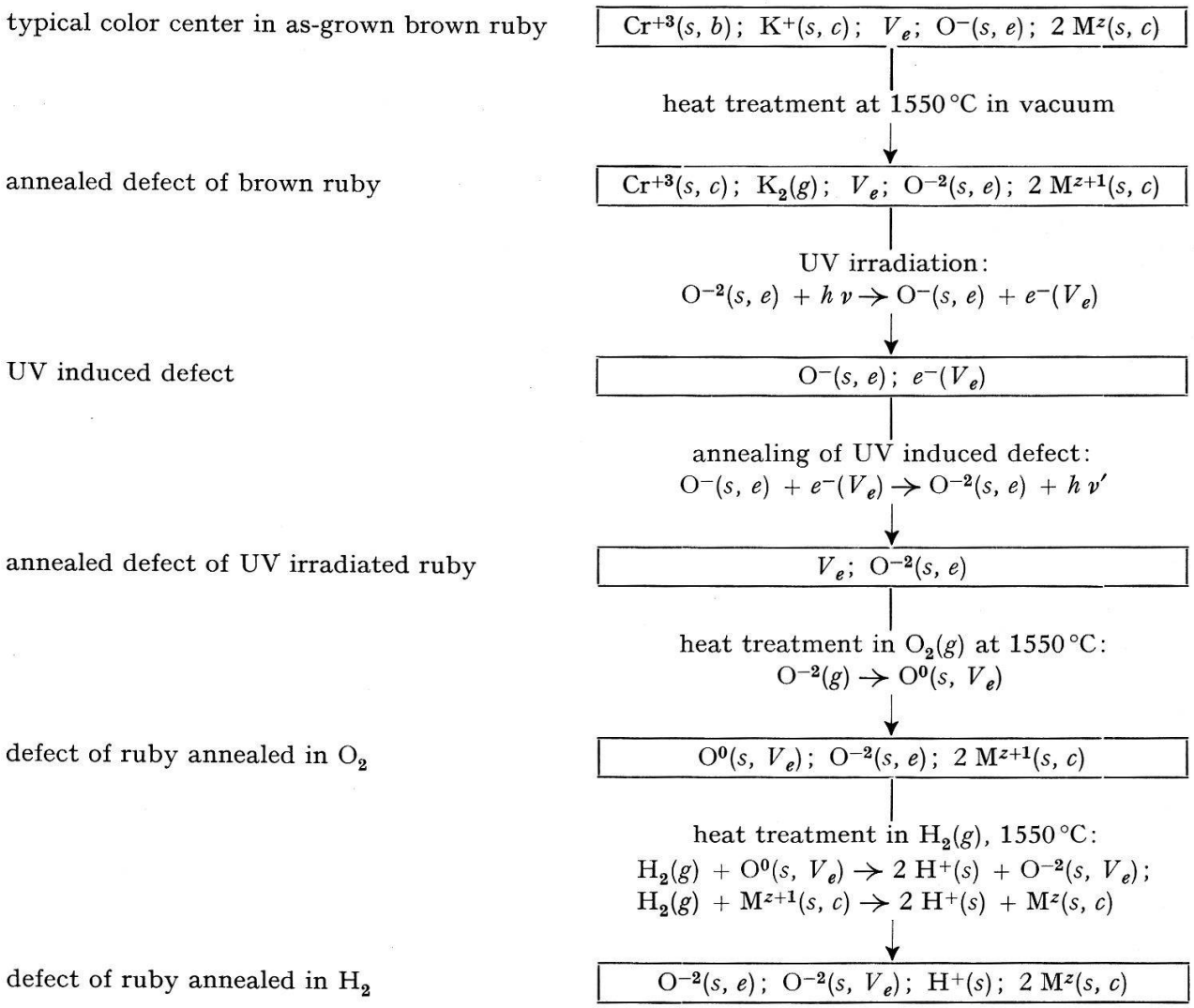

Figure 9
Schematic representation of the typical color centers in brown ruby

[1]) s and g designate the solid and gaseous phase, respectively.
[2]) b, c and e are the notations for the lattice sites according to Ref. [30].
[3]) V_e denotes a vacancy at site e.
[4]) M^z denotes one of the transition metal ions which may participate in redox reactions.
[5]) The annealing temperature for the UV induced defects is approximately 600 °C (see section 3.3).

Table 4
Thermodynamic data of gaseous species[1])

Reaction	$\Delta H^0(0)$ [kcal/mole]	Reaction	$\Delta H^0(0)$ [kcal/mole]
$^1/_2\ O_2(g) \rightarrow O(g)$	58.6	$K(g) \rightarrow K^+(g) + e^-$	100.0
$O(g) + 2\ e^- \rightarrow O^{-2}(g)$	170	$2\ K(g) \rightarrow K_2(g)$	−11
$O^-(g) + e^- \rightarrow O^{-2}(g)$	240.8	$Na(g) \rightarrow Na^+(g) + e^-$	120.0
$H_2(g) \rightarrow 2\ H^+(g) + 2\ e^-$	734	$2\ Na(g) \rightarrow Na_2(g)$	−18
$M^z(g) \rightarrow M^{z+1}(g) + e^-$	$330 \cdot z^2$)		

[1]) See Ref. [24–26].
[2]) Approximately for all transition metal ions considered in this work.

lines. One therefore may conclude that the proton actually is located unsymmetrically on the O^{-2}–O^{-2} line. The upper limits listed in Table 5 refer to the value of the potential at the saddle point. If a OH distance similar to the bond length of the free ion OH^- is assumed, then all reaction energies involved would, according to Figure 10, be reduced by at least 10 eV. This is considered as an explanation for the fact that process (2) in Table 5 is easily carried out experimentally in both directions.

Table 5
Gas-solid state reactions pertinent to defect brown rubies

Reaction[a])		Reaction energy at 0 K: $\Delta U^0(0)$
(1)	$H_2(g) + O^0(s, e) + O^{-2}(s, e) \rightarrow 2\ H^+(s) + 2\ O^{-2}(s, e)$	− 11 eV[1])
(2)	$H_2(g) + M^{z+1}(s, c) \rightarrow 2\ H^+(s) + M^z(s, c)$	+ 21 eV[1])
(3)	$O_2(g) \rightarrow 2\ O^0(s, e)$	− 0.5 eV
(4)	$O^{-2}(s, e) + 2\ H^+(s) \rightarrow H_2O(g)$	− 5.7 eV
(5)	$M^z(s, c) + H^+(s) \rightarrow M^{z+1}(s, c) + {}^1/_2\ H_2(g)$	$(-\ 54 + z \cdot 14.3)$ eV[2])
(6)	$O^-(s, e) + K^+(s, c) + 2\ M^z(s, c) + Cr^{+3}(s, b)$ $\rightarrow {}^1/_2\ K_2(g) + O^{-2}(s, e) + 2\ M^{z+1}(s, c) + Cr^{+3}(s, c)$	− 103 eV[3])

[a]) g and s designate the gaseous and the solid phase, respectively. The second letter, if present, designates the lattice site according to Ref. [30].
[1]) See remark in the text.
[2]) Approximately for all transition metal ions.
[3]) Value for $z = 2$; for $z = 1$ one obtains − 132 eV and for $z = 3$ one obtains − 74 eV.

An other comment is in order with respect to the reaction energy of process (3), which involves the incorporation of an uncharged O atom in a vacancy at a O^{-2} site. For the partial process $O(g) \rightarrow O(s, V_e)$[4]), $\Delta U^0(0)$ is equal to the crystal field energy of an O atom for the O^{-2} site. Its value, calculated from our lattice model, is given in Table 6.

[4]) V_e denotes a vacant e site.

Table 6
Lattice potentials at various sites of the corundum structure

Site[1])	Rhombohedral coordinates[4])	l	m	Coefficient c_{lm}[2])[3]) Real part	Imag. part
		0	0	− 8.800	0
		2	0	+ 0.0665607	0
c	0.105/0.105/0.105	4	− 3	− 0.0666432	+ 0.0512600
		4	0	+ 0.1687916	0
		4	3	+ 0.0666432	+ 0.0512600
		0	0	− 0.303167	0
		2	0	+ 1.016783	0
b	+ 0.25/+ 0.25/+ 0.25	4	− 3	− 0.0603529	0
		4	0	+ 0.4896426	0
		4	3	+ 0.0603529	0
		0	0	+ 6.7247	0
		1	− 1	+ 0.0100001	+ 1.358487
		1	0	0	0
		1	1	− 0.0100001	+ 1.358487
e	0.303/− 0.303/0	2	− 2	+ 0.0215624	+ 0.399861
		2	− 1	+ 0.2217505	+ 0.1691132
		2	0	+ 0.0857346	0
		2	1	− 0.2217505	+ 0.1691132
		2	2	+ 0.0215624	− 0.399861

[1]) The notation for the sites is as given in Ref. [30].
[2]) c_{lm} are the coefficients of the expansion $V(r, \vartheta, \varphi) = e_0 \sum_{l,m} c_{lm}\, r^l\, Y_l^m(\vartheta, \varphi)$ for the lattice potential. Their dimension is $\text{Å}^{-(l+1)}$.
[3]) Only those coefficients are given, which are necessary for a certain site symmetry and a certain electron configuration.
[4]) The structure as given by Ref. [27] has been used.

4.3 As a model for UV induced defects produced by process (2) in Figure 9, $O^-(s, e)$ is suggested[5]). Crystal field states for O^- on O^{-2} sites have been calculated by several authors. Bartram et al. [8] have used this model combined with a charge deficient cation for defects produced by gamma and neutron irradiation, which have similar VIS absorption bands as do the UV induced defects. A more complex structure involving O^{-2} and O^- has been suggested by Maruyama [29]. The model by Bartram appears to be suitable also for the UV defects and is therefore used here.

4.4 *Crystal Field Spectrum of Cr^{+3} at Interstitial Site*

4.4.1 Computation of the crystal field potential at various sites of the corundum structure.

The model of the defect of brown ruby presumes the existence of Cr^{+3} on the interstitial site[6]). For comparison with experiments the crystal field spectrum of Cr^{+3}

[5]) For the notation of the lattice site, see Ref. [30].
[6]) In Wykoff notation this site is $(b, \bar{3})$, cf. Ref. [30].

at this site is required. As mentionned above the crystal potential at other sites than the interstitial is also needed (c.f. section 4.2). Therefore rather extensive computations of crystal field potentials have been made, based on the following assumptions:

i. the sapphire lattice is considered as a point charge system with the ion coordinates as given by Newnham and de Haan [27]. Induced dipole and multipole contributions to the electrostatic potential were omitted. Several authors have included such contributions [31–33], which in some cases were found to be surprisingly high. However, the fields computed in this work are used mainly as a basis for comparisons. It therefore may be expected that consideration of higher terms would not change our conclusions.

ii. multipole expansion coefficients at the sites listed in Table 6 were computed numerically by summation over a nearly spherically shaped region containing up to 6000 rhombohedral unit cells.

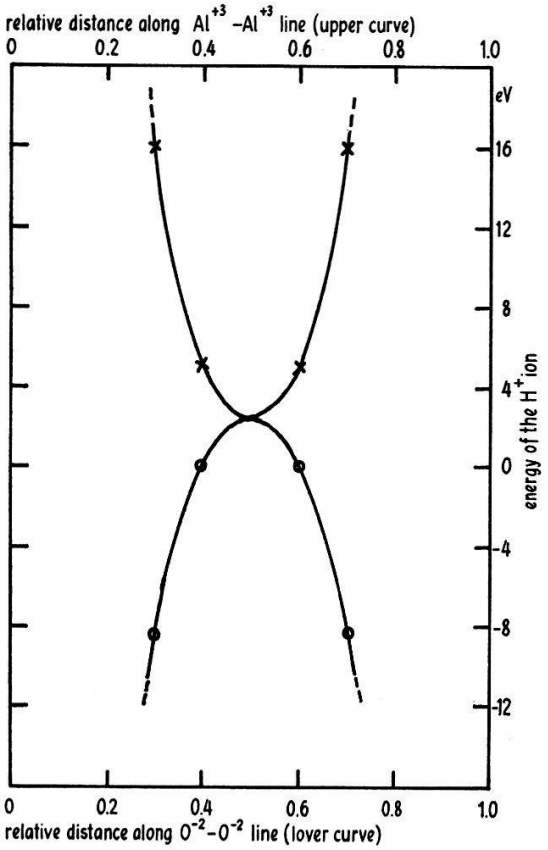

Figure 10
Crystal field energy of H^+ along the lines joining two O^{-2} ions and two Al^{+3} ions, respectively. The rhombohedral coordinates of the sites, on which these computations were based, are 0.895/−0.105/−0.105 and 0.605/0.605/−0.395 for the Al^{+3} sites, and 0.5/0.197/−0.197 and 1.0/0.303/−0.303 for the O^{-2} sites.

Table 6 shows the results. A few comments seem to be in order: The well known convergence difficulties for the unipole terms were observed even for this large summation region (50 Å radius), resulting in an uncertainity for the monopole term of approx. 2%. It should perhaps be mentionned that the unipole terms depend critically on the summation sequence. However, the Madelung constant derived from the unipole terms is nearly independent of the summation process. The higher terms c_{lm}, $l \geqslant 1$ are much less sensitive to the sequence and region of summation.

4.4.2 *Crystal Field Spectrum of Cr^{+3} at Site $(b, \bar{3})$*

For derivation of the crystal field spectrum the following assumptions were made:

i. the ion Cr^{+3} is subject to the electrostatic crystal field only, as calculated sub 4.4.1; no overlap effects are considered.

ii. for the free ion all 3 d^3 configurations are used, resulting in a base consisting of 120 Slater determinants.

iii. Spin-orbitals were constructed from numerically given SCF-Hartree-Fock orbitals [34]. By using the Condon-Shortley theorems [35] each matrix element was reduced to one electron integrals. The resulting radial integrals $\langle r^l \rangle$ were obtained by numerical integration.

iv. the crystal field energy matrix was calculated in a $|J\ J_3\rangle$ base. This base was constructed from the Slater base by first constructing base functions $|L\ S\ L_3\ S_3\rangle$, which then were coupled by the usual vector coupling coefficients to obtain the $|J\ J_3\rangle$ base functions [36]. The whole process was made by appropriate computer programs.

v. since in the $|J\ J_3\rangle$ base the LS-coupling operator [35] is diagonal, its matrix elements for the free ion can be used directly.

vi. the relevant site group for the ion Cr^{+3} on site b is the double group C^*_{3i}, which is isomorphous to C_6. In Table 7 the irreducible representations of C^*_{3i} are given together with the transformation properties of the electric dipole moment operator. The $|J\ J_3\rangle$ base functions may directly be used as base functions of the irreducible representations Γ_{J3} of C^*_{3i}. Inspection of the $|J\ J_3\rangle$ base functions shows that only the representations $\Gamma_{1/2}$, $\Gamma_{3/2}$ and $\Gamma_{5/2}$ occur; as a consequence the energy matrix is factorized into three blocks, which were diagonalized numerically.

As a check for the accuracy of the crystal field spectrum of Cr^{+3} on site b the well known spectrum at site c, based on the crystal field at this site (see Table 6) has been computed. For the two bands in the VIS region centers of transitions at 420 and 600 nm were obtained as compared with 400 nm and 560 nm, respectively, obtained experimentally.

Table 7
Irreducible representations of the double group C^*_{3i}

	E	$U(\alpha)$	$U(2\,\alpha)$	$U(3\,\alpha)$	$U(4\,\alpha)$	$U(5\,\alpha)$
Γ_0	1	1	1	1	1	1
$\Gamma_{1/2}$	1	k	k^2	k^3	k^4	k^5
Γ_1	1	k^2	k^4	1	k^2	k^4
$\Gamma_{3/2}$	1	k^3	1	k^3	1	k^3
Γ_2	1	k^4	k^2	1	k^4	k^2
$\Gamma_{5/2}$	1	k^5	k^4	k^3	k^2	k

$\alpha = 2\,\pi/3 \qquad k = \exp[i\,\pi/3]$

Table 8
Calculated transitions in the UV/VIS region, which explain the observed 315 nm band [31750 cm^{-1}].

Energy of level [cm^{-1}]	Transition energy [cm^{-1}]	Assignment to free ion levels
54984	32444	$^4F - {}^4P$
54964	32424	$^4F - {}^4P$
54861	32321	$^4F - {}^4P$
54761	32221	$^4F - {}^4P$
54727	32187	$^4F - {}^4P$
54656	32116	$^4F - {}^4P$
54646	32106	$^4F - {}^4P$

The resulting energy level pattern for Cr^{+3} on site b is shown in Figure 11[7]). Selection rules for electric dipole transitions under the site group C_{3i}^* may be obtained from Table 7 in the usual way. Inspection of the level pattern (Figure 11) reveals,

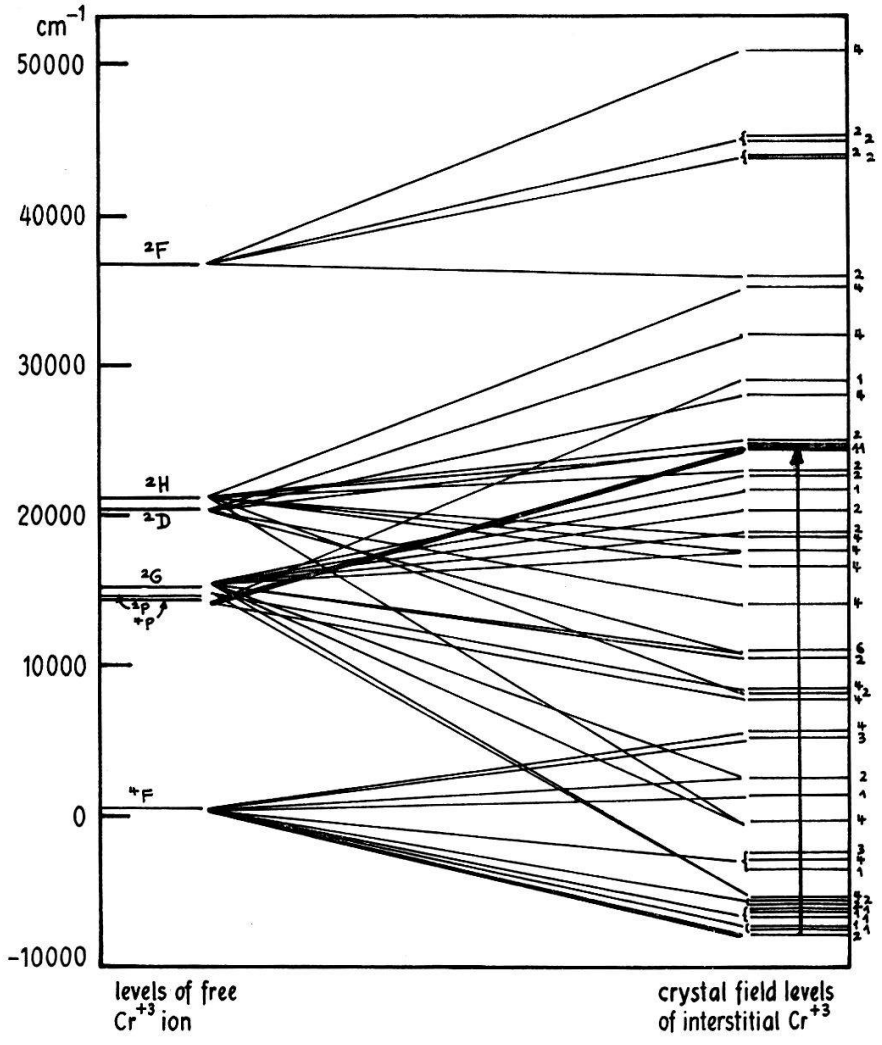

Figure 11
Energy level diagram for interstitial Cr^{+3}.
Remark: The numbers at the right side of the diagram denote the number of levels involved in each of the horizontal straight lines. It has nothing to do with a physical degeneracy.

[7]) Figure 11 seems to contain levels apparently violating the Kramers theorem. This however is to be traced back to numerical errors.

that the optical transitions collected in Table 8 may be considered as an explanation for the 315 nm absorption which was observed experimentally.

It should be pointed out that these transitions, predicted in the region 32100 to 32440 cm^{-1} (312 to 308 nm), are the only ones in the UV-VIS region of the crystal field pattern Figure 11, which are both symmetry and spin allowed. This result, together with the satisfactory agreement of calculated and observed transition frequencies, is considered as a significant support of the interpretation of the typical defect of brown ruby as crystal field transitions of Cr^{+3} on interstitials.

One remark should be made concerning the results of the ESR measurements (see section 3.5). The ESR spectrum of Cr^{+3} at the interstitial site is not known and so far has not yet been found in brown rubies, where it should be present. Explanation of this may be based on the fact, that the concentration of the defect in brown ruby does not exceed approximately 50 ppm according to the impurity analysis given in Table 1. Furthermore, the symmetry groups of substitutional (c) and interstitial sites (b) are C_3^* and C_{3i}^*, respectively, both isomorphic to C_6. Differences in the ESR spectrum could therefore result mainly from the different g-tensors produced by different crystal fields in both sites. However, no theoretical study of this point has so far been made.

Acknowledgment

We wish to express our gratitude to the following persons, who gave valuable assistance to this work

- Messrs. B. Gächter and H. Blum for measurement of thermoluminescence spectra,
- Mr. J. Keller and the computation center staff of the ETH for programming and numerical computation,
- Dr. H. Preis and Mr. A. Esenwein, EMPA, Dübendorf/Zurich, for microprobe analytical work,
- Dr. A. Wyttenbach, EIR, Würenlingen, for activation analysis experiments.

REFERENCES

[1] R. A. Hunt and R. H. Schuler, Phys. Rev. *89*, 664 (1953).
[2] P. W. Levy, Disc. Farad. Soc. *31*, 118 (1961).
[3] P. W. Levy, Phys. Rev. *123*, 1226 (1961).
[4] E. W. J. Mitchell, J. D. Rigden and P. D. Townsend, Phil. Mag. *5*, 1013 (1960).
[5] A. F. Gabrysh, H. Eyring, V. Le Febre and M. D. Evans, J. Appl. Phys. *33*, 3389 (1962).
[6] A. F. Gabrish, J. M. Kennedy, H. Eyring and V. R. Johnson, Phys. Rev. *131*, 1543 (1963).
[7] F. T. Gamble, R. H. Bartram, C. G. Young, O. R. Gilliam and P. W. Levy, Phys. Rev. *134*, A589 (1964).
[8] R. H. Bartram, C. E. Swenberg and J. T. Fournier, Phys. Rev. *139*, A941 (1965).
[9] B. Sujak and A. Niklas, Acta Phys. Polonica *31*, 769 (1967).
[10] B. Sujak and A. Niklas, Acta Phys. Polonica *32*, 711 (1967).
[11] H. W. Lehmann and H. H. Günthard, J. Phys. Chem. Sol *25*, 941 (1964).
[12] R. Müller and H. H. Günthard, J. Chem. Phys. *44*, 365 (1966).
[13] I. B. Cutler, J. L. Bates and P. Gibbs, Bull. Am. Phys. Soc. *2*, 300 (1957).
[14] R. C. Pastor, H. Kimura, L. Podoksik and M. A. Pearson, J. Chem. Phys. *43*, 3948 (1965).

[15] R. C. Pastor, A. C. Pastor, H. Kimura and K. Arita, J. Chem. Phys. *44*, No. 12, 4486 (1966).
[16] R. C. Pastor, J. Chem. Phys. *45*, No. 1, 321 (1966).
[17] A. C. Pastor, R. C. Pastor and B. H. Soffer, Mat. Res. Bull. *1*, 205 (1966).
[18] D. S. McClure, Solid State Physics *9*, 400 (1959).
[19] P. E. Schmid and Hs. H. Günthard, J. Appl. Math. and Phys. *17*, Fasc. 3, 404 (1966).
[20] W. J. Borer, Ph. D. thesis, Zürich (1969).
[21] R. Urbach, *Storage and Release of Light by Phosphors*, Cornell Symposium, 115, Wyley, N.Y.
[22] G. Bonfiglioli, P. Brovetto and C. Cortese, Phys. Rev. *114*, 951 (1956).
[23] A. Halperin and A. A. Braner, Phys. Rev. *117*, 408 (1960).
[24] National Bureau of Standards, Circular 500, *Selected Values of Chemical Thermodynamic Properties*, Part I, Washington (1961).
[25] J. A. A. Ketelaar, *Chemische Konstitution*, Braunschweig (1964).
[26] A. G. Gaydon, *Dissociation Energies and Spectra of Diatomic Molecules*, London (1968) (Chapman & Hall).
[27] R. E. Newnham and Y. M. de Haan, Z. Krist. *117*, 235 (1962).
[28] H. H. Grimes and J. H. Rice, J. Phys. Chem. Sol. *29*, 1481 (1968).
[29] T. Maruyama, Y. Matsuda, H. Kon and H. Yonemitsu, J. Phys. Soc. Japan *18*, Suppl. 2, *315* (1963).
[30] *Internat. Tables for X-ray Crystallography*, Vol. I, p. 274, Birmingham (1952).
[31] J. O. Artman and J. C. Murphy, Phys. Rev. *135*, 1622 (1964).
[32] R. R. Sharma and T. P. Das, J. Chem. Phys. *41*, 3581 (1964).
[33] S. Hafner and M. Raymond, J. Chem. Phys. *49*, 3570 (1968).
[34] C. W. Nestor, Computer Program for Hartree-Fock Wavefunctions, Oak Ridge National Laboratory.
[35] E. U. Condon and G. H. Shortley, *The Theory of Atomic Spectra*, p. 169 (1957).
[36] E. P. Wigner, *Group Theory*, p. 192, Academic Press N.Y. (1964).